Review of Scientific Instruments ARTICLE pubs.aip.org/aip/rsi

Lock-in infrared thermography: Phase analysis for rapid, wide-range thermal conductivity measurements

Cite as: Rev. Sci. Instrum. 97, 094905 (2026); doi: 10.1063/5.0346125
Submitted: 1 June 2026 • Accepted: 6 September 2026 •
Published Online: 29 September 2026

View Online Export Citation CrossMark

Ethan A. Scott,[1,a] Jeffrey L. Braun,[2] Jessica Reyes,[1] Bruce Bolliger,[3] Terrence Soares,[3] John T. Gaskins,[2] Marko J. Tadjer,[4] and Patrick E. Hopkins[1,2,5,6]

AFFILIATIONS

[1] Department of Mechanical and Aerospace Engineering, University of Virginia, Charlottesville, Virginia 22904, USA
[2] Laser Thermal Analysis, Inc., 937 2nd St SE, Charlottesville, Virginia 22902, USA
[3] Element Six Technologies US Corp., Santa Clara, California 95054, USA
[4] US Naval Research Laboratory, Washington, District of Columbia 20375, USA
[5] Department of Materials Science and Engineering, University of Virginia, Charlottesville, Virginia 22904, USA
[6] Department of Physics, University of Virginia, Charlottesville, Virginia 22904, USA

[a] **Author to whom correspondence should be addressed:** eascott@virginia.edu

ABSTRACT

We report on a phase-based lock-in thermography approach, combined with a multilayered thermal model (often employed in thermoreflectance analysis), to measure the thermal conductivity of a variety of materials. The spatial distribution of the material's thermal phase is monitored with an infrared camera, which is locked into the frequency of a modulated laser used to heat the material. This phase distribution is then fit with a thermal model, in which properties such as thermal conductivity are extracted as fit parameters. This approach enables non-contact, front-side measurements, which are insensitive to surface roughness. The technique does not strictly require the application of a transducer layer, but we highlight the practical benefits of applying a removable adhesive layer to serve as a near-surface absorber. We demonstrate the efficacy of the method by measuring materials with thermal conductivities that span more than three orders of magnitude (~1 to >2000 W m^{-1} K^{-1}).

© 2026 Author(s). All article content, except where otherwise noted, is licensed under a Creative Commons Attribution (CC BY) license (https://creativecommons.org/licenses/by/4.0/). https://doi.org/10.1063/5.0346125

I. INTRODUCTION

Material thermal performance is integral to engineering design. From raw construction material to synthetic materials for advanced technological applications, heat transfer plays a key role. Therefore, knowledge of properties such as thermal conductivity is essential for accurate prediction of the performance of an engineering design.

There are many approaches to measuring thermal conductivity, including contact, non-contact, optothermal, electrothermal, steady-state, and transient techniques.[1] Among these, laser-based methods have become particularly attractive because they are non-contact, minimizing sample preparation and often enabling non-destructive measurements. Despite these shared advantages, individual laser-based techniques differ substantially in sample preparation requirements, spatial scale, thermal modeling capability, practical measurement range, and relative experimental complexity. For example, Table I summarizes several representative laser-based approaches for thermal conductivity measurements.

In consideration of the trade-offs that exist among these techniques, Braun *et al.*[7] outlined experimental characteristics that are most useful in practice. Among these, the most important ones are (1) simplicity in use and analysis, (2) relevance to a wide range of materials and thermal conductivities, (3) high-throughput capability, (4) accuracy and repeatability, (5) localized nature, and (6) tolerance to sample geometry and surface condition. To this end, a thermo-optical plane source (TOPS) method was developed. The

© Author(s) 2026

TABLE I. Comparison of representative laser-based thermal conductivity measurement techniques, including thermoreflectance (TDTR, FDTR, and SSTR), laser flash analysis (LFA), thermo-optical plane source (TOPS), and conventional LIT techniques. We note that the listed table values are representative values from the cited literature and are not intended as fundamental measurement limits.

Technique	Sample prep.	Detector	Meas. scale	Layered model	κ range (W m^{-1} K^{-1})	Rel. complexity
TDTR/FDTR[1]	Metal transducer; polished	Photodiode	Point (μm)	Standard	~0.1–2000	High
SSTR[1,2]	Metal transducer; polished	Photodiode	Point (μm)	Standard	~0.1–2000	Mod.–high
LFA[3–6]	Front/back prep.; coatings often applied	IR detector	Bulk (mm–cm)	Possible	~0.1–2000	Moderate
TOPS[7]	Calibrated absorbing layer	IR camera	Area (mm)	Standard	0.03–60	Mod.–low
LIT[8–14]	Minimal; absorbing layer optional	IR camera	Area (mm)	Limited	0.03–400	Low
This work	Minimal; absorbing layer optional	IR camera	Area (mm)	Standard	~1–2000	Low

TOPS method employs a robust infrared detection scheme, which analyzes the magnitude of a material's temperature rise as a function of incident laser power in order to directly measure thermal conductivity. While the approach satisfies many of the aforementioned characteristics, it is best suited for low thermal conductivity materials[7] (generally materials with $\kappa < 100$ W m^{-1} K^{-1}).

In this work, we combine concepts from the TOPS technique, lock-in infrared thermography (LIT), and continuous-wave thermoreflectance approaches[2,15] to enhance the capabilities of non-contact infrared-based measurements. This method pushes the upper limit of measurable thermal conductivities while maintaining many of the aforementioned measurement characteristics. The resultant technique is non-contact and non-destructive, requires only single-sided optical access, does not require a polished surface, does not strictly require an absorbing layer/transducer, and enables quantitative measurements of materials with thermal conductivities exceeding 2000 W m^{-1} K^{-1}.

II. BACKGROUND AND THEORY

There have been numerous implementations of LIT. A few recent examples are demonstrated in Refs. 8–14. Despite the variations among these implementations, the common underlying principle of operation is that a material is periodically heated (usually with a modulated laser source) and the thermal response is captured with an infrared (IR) camera and processed via lock-in demodulation to extract the magnitude and phase at the modulation frequency. The data are then analyzed to extract thermal properties. The strength of the technique comes from lock-in amplification, which enhances the signal-to-noise ratio, allowing for the detection of small temperature variations. A significant benefit of phase analysis is that, in contrast to magnitude, the absorbed power does not need to be known. This reduces the number of model parameters, and in part, is why phase is preferentially modeled in other lock-in based thermal metrologies, such as time-domain[16] or frequency-domain thermoreflectance.[15,17]

In this approach, we extract thermal properties from the phase by employing a model similar to that used for thermoreflectance.[2,15,18] That is, the radial heat diffusion equation is solved for structures in response to a periodic, Gaussian heat source. A benefit of this modeling approach is the ability to accommodate structures with an arbitrary number of layers, thus allowing for consideration of thermo-optic transducer (absorbing) layers or systems that consist of film(s) on a substrate.

We first solve for the complex temperature $\tilde{T}(r,\omega)$ in a similar manner as Refs. 2 and 19, where r is the radial distance from the center of the modulated laser heat source and ω is the angular frequency. From this, we calculate the thermal phase as $\theta(r,\omega) = \text{atan2}\left(Y(r,\omega), X(r,\omega)\right)$, where $X(r,\omega) \equiv \text{Re}[\tilde{T}(r,\omega)]$ and $Y(r,\omega) \equiv \text{Im}[\tilde{T}(r,\omega)]$. The difference between the modeled and the measured thermal phase is then minimized with a least-squares routine in which properties of interest are treated as adjustable parameters. A full description of the mathematical model is provided in Appendix A.

III. EXPERIMENTAL DETAILS

A schematic of the experimental layout is shown in Fig. 1. The setup consists of a sample, which is periodically heated by a laser and is monitored with a lock-in IR camera. The camera captures the spatial distribution of the thermal phase, which is then output to a computer for refinement and analysis.

We utilize a Coherent Verdi V5 continuous-wave laser, which has a central wavelength of 532 nm and maximum optical power output of 5 W. The laser is modulated at a desired frequency with a Stanford Research Systems Model SR542 Precision Optical Chopper. Lenses are used to adjust the laser spot size at the sample surface. We then measure the focused spot size with a Thorlabs BP209-VIS beam profiler. We adjust the laser power to provide a sufficient signal-to-noise ratio while limiting self-heating. In this implementation, we limit the first-harmonic temperature amplitude to $|\tilde{T}(r=0,\omega)| < 20$ K, which results in an area-averaged lock-in temperature amplitude of less than 1 K. Calculation of the area-averaged value is detailed in Appendix B.

The thermal phase of the sample is monitored with an InfraTec ImageIR 8380 IR camera, which is a mid-wave IR camera that has a 640 × 512 pixel resolution and ≤20 mK temperature resolution. We lock into the heating frequency of the sample by diverting a small percentage of the laser with a beam sampler (Thorlabs BSF10-A) and directing it into a photodetector (Thorlabs DET10A). The DET10A output is converted into a transistor–transistor logic (TTL) compatible signal with a comparator (Pulse Research Lab PRL-350TTL). This is then supplied as the reference signal for the IR camera with a

© Author(s) 2026

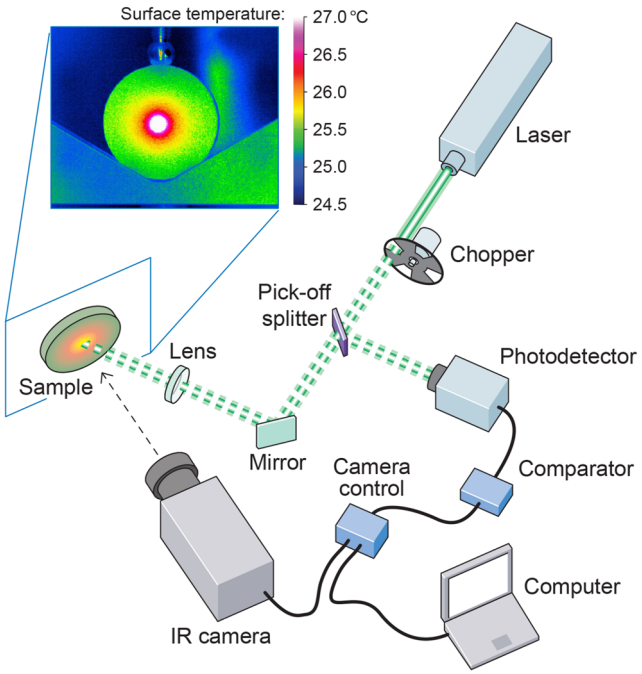


FIG. 1. Schematic of the experimental setup.

camera control module. The control module shown in Fig. 1 represents a combination of the InfraTec Active Thermography Control Module and a breakout box. The thermal phase is acquired over a specified time or number of periods and output to a tabulated data file, which is then analyzed with a thermal model. We generally collect 100 periods per measurement using a camera frame rate of 200 Hz.

IV. RESULTS AND DISCUSSION

A. Sample measurements

The spatially distributed thermal phase is radially symmetric for an isotropic material heated with a circular (Gaussian) beam. To minimize variation in the data that occurs from sample imperfections, we take a radial average of the phase for a vector that extends outward from the center of the laser-heated region to the edge of a user-defined region of interest (ROI) and is rotated 360° about the center point. The center point corresponds to the point of the least negative phase. We use a peak-finding algorithm to automate center point determination. The radius of the ROI is typically on the order of millimeters, but is a function of the laser spot size and sample properties. For example, the spatial extent of the lateral temperature rise is higher for more conductive materials. Figures 2(a)–2(e) demonstrates this, showing the spatially distributed phase and the defined ROI for a variety of samples. The radially averaged phase is shown directly beneath the corresponding contour image.

All of the phase plots in Fig. 2 show a symmetric profile about $r = 0$ mm, in which the phase monotonically decreases as r is increased. This indicates that the temperature rise becomes increasingly out of phase with the frequency of the heating laser as the distance from the center of the heat source increases. For a given heating frequency, this offset in phase is more pronounced for materials with lower thermal conductivity. This is indicated by the slopes of the curves in Fig. 2 where each panel shows a material with successively increasing thermal conductivity. If the slope is sufficiently large, additional data processing is required. For example, the camera records the thermal phase for $-180° \leq \theta \leq 180°$. If the thermal phase is lower than this threshold, the phase is wrapped and must be manually corrected by subtracting 180° from the apparent value; data points within the discontinuity of the phase wrap are discarded. An example of this is shown for the SiO_2 sample in Fig. 2.

We note that the plots in Fig. 2 show the thermal phase for materials coated with a thin, optically absorbent adhesive layer. However, to be clear, this layer is not strictly necessary if the irradiated material is absorptive of the incident laser power. However, absorbing layers have been demonstrated in prior reports[7] as a means to improve absorption of the incident beam, which ultimately reduces the laser output power requirement. This is particularly useful for materials that are highly thermally conductive, optically transmissive, or reflective of the heating laser. In those cases, we use a black polymer-based absorber, which is a 5 μm thick tape consisting of a black polyethylene terephthalate (PET) film with an acrylic adhesive. While this adds an extra step, this transducer application is faster than the metallization required for thermoreflectance and is easier to remove by peeling or dissolving in acetone.

We demonstrate the effect of the absorber layer by comparing the apparent thermal conductivity of a material measured with and without an absorber layer. In particular, we measure silicon wafers [University Wafer, (100), SSP, P/B 1-100 Ω-cm, 724 μm thick] that were cleaved, 1 in. on a side. LIT measurements were performed on each sample using a laser spot size of 880 μm ($1/e^2$ diameter), chopped at a frequency of 2 Hz. Figures 3(a) and 3(b) show the radially averaged phase of a bare silicon wafer and a PET-coated wafer, respectively. For reference, we also measure a piece of the silicon with PET on the unpolished side. The RMS roughness was measured with a Bruker DektakXT stylus profilometer as 1.8 ± 0.3 μm. Figures 3(d)–3(f) show the fitted thermal conductivity of each sample and the associated uncertainty. In each case, the thermal conductivity is within uncertainty of the other samples, indicating minimal difference in the effect of sample preparation or surface condition. This is attributed to the spatial extent of the measurement. In contrast, thermoreflectance generally probes a region that is several microns in diameter and is tolerant to tens of nanometers of RMS roughness.[16] LIT data are averaged over an area of several square millimeters and is tolerant to surface roughness on the order of a micron, compatible with unpolished wafers.

Regarding the uncertainty of the model fit, we apply the same approach used in thermoreflectance. That is, we add in quadrature the uncertainty from the spot-to-spot variation, uncertainty from the least squares model fit (employing a 95% confidence interval), and uncertainty in the fixed model parameters (accounted for with Monte Carlo analysis[17,20]). For the PET layer, we assume an average thermal conductivity of 0.28 W m^{-1} K^{-1} and average heat capacity of 1.62 MJ m^{-3} K^{-1}, which are representative of thermoplastic polymers.[21] We note, however, that the thermal properties of this transducer layer have an insignificant effect on the thermal model, evidenced also by the similarity in data between samples with and without the transducer, as shown in Fig. 3. For the interface between

© Author(s) 2026

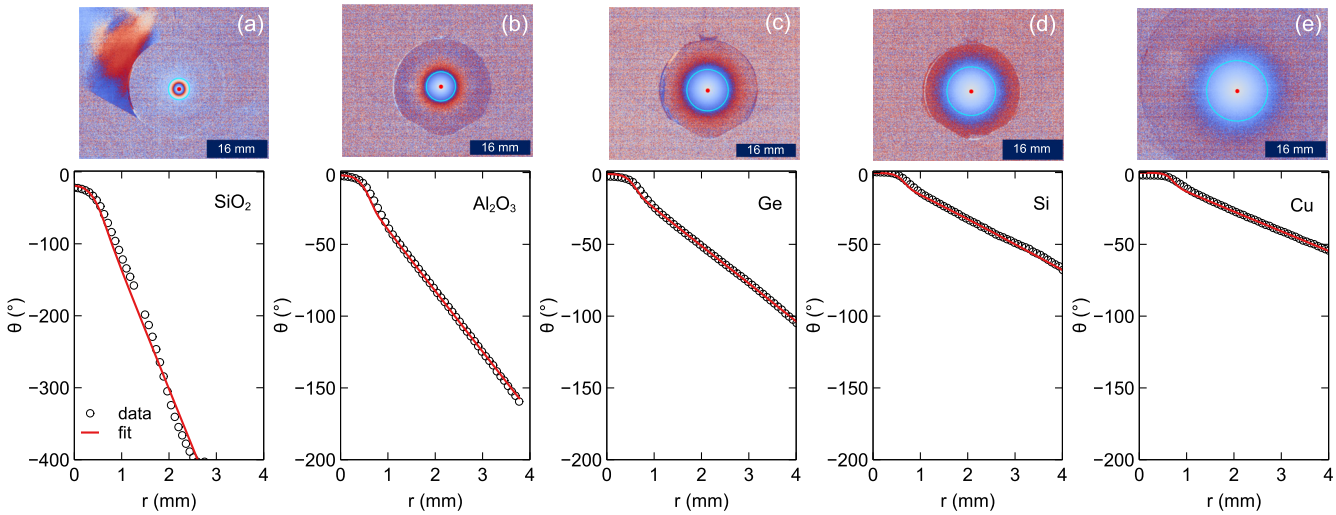


FIG. 2. Example thermal phase images, as monitored by using the IR camera. The corresponding radial average of the phase is displayed below each image along with the best-fit model for each curve.

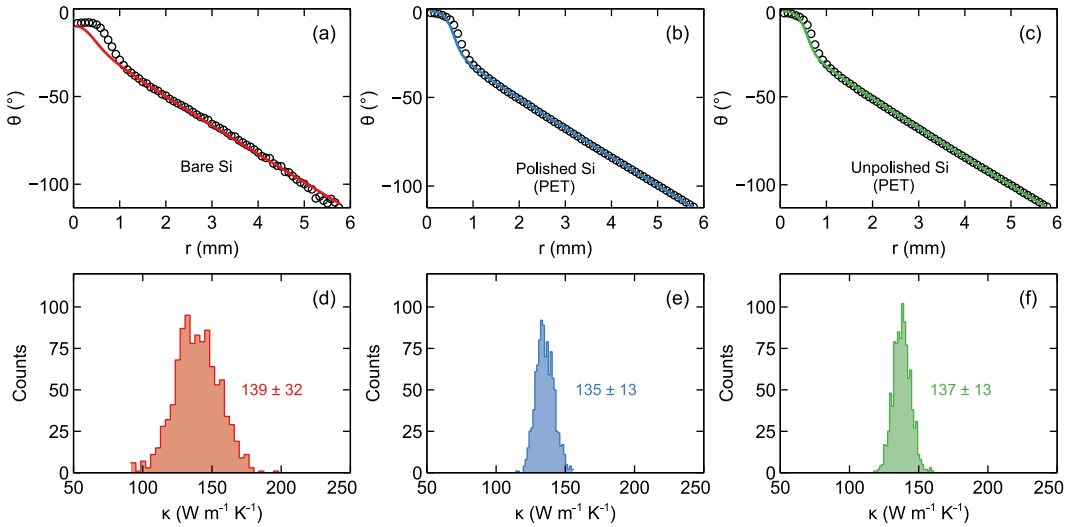


FIG. 3. Fitted phase data from a bare Si wafer (a), Si wafer with PET on the polished side (b), and a Si wafer with PET on the unpolished side (c). Panels (d)–(f) show associated histograms of the fitted thermal conductivity from Monte Carlo simulation.

the PET layer and the sample substrate, we assume a low interface conductance of $G = 1$ MW m^{-2} K^{-1}, but again note that there is minimal sensitivity to the assumed input (which we address through sensitivity analysis in Sec. IV C). For Monte Carlo simulation of fixed parameters, we account for 10% variability in the assumed thermal conductivity, heat capacity, and interface conductance of the PET layer, and one micron variability in PET thickness. We assume a 2% uncertainty in the assumed substrate volumetric heat capacity. We assume 10% uncertainty in the measured beam diameter and also account for uncertainty in the measured pixel density. We also account for uncertainty in the thermal absorption depth of the incident laser.[22] We conservatively account for this by varying the nominal absorption depth over the entire thickness of the PET film, but observe a negligible effect. Ultimately, we find that uncertainty in the measured camera pixel density is the largest source of measurement uncertainty.

Figures 3(d)–3(f) shows the results of 1000 Monte Carlo fit iterations for the phase models of Figs. 3(a)–3(c), respectively. The total uncertainty is ~10% for the fitted thermal conductivity for the Si with PET. In contrast, there is higher variability in the measured phase of the bare wafer due to lower absorption, which yields a larger distribution in the Monte Carlo simulation results. This also necessitates

© Author(s) 2026

increased laser power; an incident laser power of 0.35 W was applied to the samples with PET whereas 2.6 W was applied to the bare Si wafer.

B. Bounds of operation

Outside thermal model considerations, precautions must be taken with regard to sample preparation and camera configuration. In an ideal scenario, samples would be infinitely large, such that there is no spatial limitation to thermal diffusion. In addition, the camera would have an infinitely high sampling rate to avoid any aliasing effects. In reality, samples are of a finite size, which limits the extent of thermal spreading and the range over which the thermal phase can be averaged for analysis. As a result, confinement of heat in small samples can lead to offsets in the thermal phase observed by using the IR camera. One solution is to restrict the extent of the thermal spreading within a given period of time. This can be achieved by increasing the frequency of the laser modulation.[23] Slow modulation results in greater thermal diffusion length and vice-versa. However, the frame rate of the camera is limited, which imposes practical limits on the modulation frequency. In our case, the frame rate is limited to 200 Hz, which is the product of the LIT frequency (periods per second) and the sampling rate (frames per period). We find that noticeable offsets in the phase occur at sampling rates below ~7 frames per period, and thus, we are generally limited to LIT frequencies below 30 Hz, although the exact limit depends on the particular sample. Use of a higher modulation frequency is preferable as it reduces the measurement duration. However, frequencies greater than ~1 Hz are generally not required unless the sample is highly thermally conductive (hundreds of W m^{-1} K^{-1}) or the sample has a low or moderate thermal conductivity and is small (side lengths ≤1 cm).

We demonstrate these effects by measuring the apparent thermal conductivity of a sample as a function of fit radius, modulation frequency, and sample size. We perform these measurements on the same silicon used for the tests shown in Fig. 3. Figure 4(a) shows the effect of a fitted radius. In this case, there is minimal difference in fitted thermal conductivity for $r \geq 2$ mm. For smaller radii, the thermal model is largely insensitive to the thermal conductivity, which we discuss in further detail in Sec. IV C.

Figure 4(b) shows the effect of modulation frequency. The laser beam was chopped at frequencies between 0.2 and 50 Hz (which are the limits of the lock-in camera in our configuration). On the low-frequency end (f < 1 Hz), we observe a reduction in the apparent thermal conductivity. We attribute this to confinement of thermal diffusion, which in turn yields an offset in the thermal phase. The effect is exacerbated as the lateral sample dimensions are reduced. For example, Fig. 4(b) also shows a silicon sample cleaved into a coupon 1 cm on a side, which yields a further-reduced thermal conductivity for a given modulation frequency below 8 Hz. As the modulation frequency is increased, there is a threshold above which the apparent thermal conductivity remains consistent. If the modulation frequency is further increased, there is an increase in the apparent thermal conductivity, which can be attributed to a combination of spatial and temporal measurement limitations. As the modulation frequency increases, the thermal diffusion length decreases and becomes confined to a smaller region surrounding the heat source. Consequently, the phase profile is represented by fewer independent pixels and the fit becomes increasingly sensitive to properties such as beam size, center location, optical resolution, and measurement noise, and less sensitive to the material thermal conductivity. At the same time, the number of camera frames recorded during each modulation cycle decreases with increasing modulation frequency. As a result, the lock-in reconstruction of the thermal waveform becomes increasingly susceptible to systematic error, further contributing to distortion of the measured phase profile and an overestimation of the apparent thermal conductivity. This effect occurs for $f \geq 20$ Hz for the Si sample shown in Fig. 4(b).

If samples are sufficiently large [e.g., the 1 in. sample shown in Fig. 4(b)], the region of consistent thermal conductivity is clear and the fitted values within this region are representative of the true material thermal conductivity. When samples are small and conductive (e.g., the 1 cm Si sample), this region may be narrow or unclear, ultimately necessitating fabrication of a larger sample. As another example, Fig. 4(c) shows the same frequency-dependent analysis of a CVD diamond wafer (E6 TM220, 33 mm diameter). The sample is similar in size to the cleaved silicon. However, it is more than an order of magnitude more thermally conductive. Therefore, we observe a modified region of consistent thermal conductivity in the region from 10 to 30 Hz, which averages to ~2490 W m^{-1} K^{-1}. Above

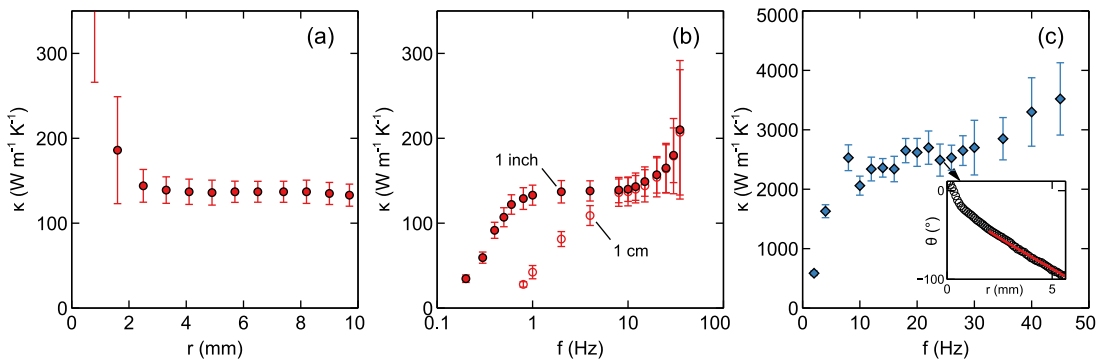


FIG. 4. Measurement parameter effects on fitted thermal conductivity. Panel (a) shows the effect of fit cutoff radius. Panels (b) and (c) show the effect of modulation frequency for Si (cleaved, 1 in. and 1 cm on a side) and diamond (33 mm, E6 TM220), respectively. The inset of panel (c) shows an example fit of diamond at 24 Hz.

© Author(s) 2026

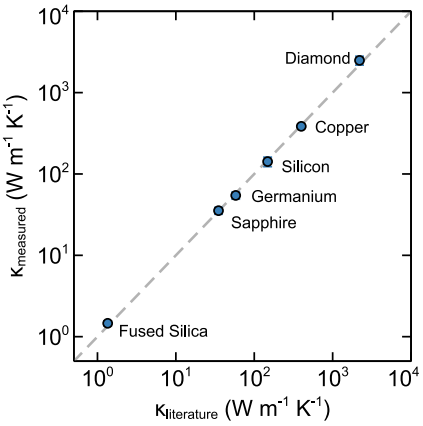


FIG. 5. Comparison of measured thermal conductivity values with those expected from the literature for a variety of bulk samples.

30 Hz, there is a similar reduction in fit quality due to modification of the apparent phase. In order to measure smaller samples of diamond, a camera with a higher frame rate would be required.

Once the camera and fit parameters are established, accurate measurements can be obtained for materials spanning a wide range of thermal conductivity. In Fig. 5, we show measurements for several bulk samples compared against their literature or manufacturer-claimed values, as tabulated in Table II. We note that all measurements shown in Fig. 5 (except for the copper and diamond) are optical windows, 1 in. in diameter, from Thorlabs. The copper sample was purchased from McMaster-Carr (part number 9103K2), and the diamond is a 33-mm-diameter wafer of the commercially available TM220. In all cases, a modulation frequency of 2 Hz was used, except for the fused silica and diamond. For low thermal conductivity materials, the thermal diffusion length is small and, therefore, a lower frequency (0.2 Hz) was used to increase the fit radius. Diamond was measured over a range of 10–30 Hz, as previously discussed. Ultimately, the measurements for each material agree, within uncertainty, with the literature or manufacturer-specified values.

C. Sensitivity considerations

Figure 4(a) demonstrates the effect of the fitted region cutoff radius: minimal changes in resultant thermal conductivity for $r \geq 2$ mm. At the other extreme, there are large errors in the apparent fitted value, which are attributed to negligible sensitivity to the substrate thermal conductivity. That is, the thermal phase is not strongly impacted by a change in apparent thermal conductivity within that region. To quantify sensitivity of the phase, S, to a given parameter, x, we define S_x using an approach similar to that of Yang *et al.*[30] for FDTR. In this case, we calculate S_x as a function of radius as $S_x(r) = \theta|_{1.1x}(r) - \theta_{0.9x}(r)$, where $\theta|_{1.1x}(r)$ and $\theta|_{0.9x}(r)$ denote the radial dependence of the thermal phase in response to positive and negative 10% perturbations in the variable of interest, respectively.

In Fig. 6, we consider parameter sensitivity for bulk materials [Figs. 6(a)–6(c)] and for a film on a substrate [Figs. 6(d)–6(f)]. In both cases, we assume that a layer of PET has been adhered to the surface. For the bulk material, we consider the sensitivity of the substrate thermal conductivity, heat capacity, and also the interface conductance between the absorber layer and substrate. In each case, we assume a 1-mm-thick substrate with default thermal properties of $\kappa = 100$ W m^{-1} K^{-1}, $C = 2$ MJ m^{-3} K^{-1}, and $G = 1$ MW m^{-2} K^{-1}. The curves in each panel show the effect of perturbing one of these parameters. With regard to substrate thermal conductivity, S_κ is minimized near $r = 0$ and becomes more pronounced as r increases. Therefore, sensitivity to κ scales with r, which underscores the benefits of larger samples, particularly for highly thermally conductive samples. This also shows that the entire radius is not needed in order to accurately fit the thermal conductivity. As long as the correct slope is established, it is sufficient to accurately fit the thermal conductivity of a bulk substrate. This approach of fitting the slope of the phase has been previously demonstrated[31,32] and can be useful if there are defected regions or aberrations in the collected phase at certain radii. For the materials measured in this study, we fit the entire radial range, except for diamond, in which case we fit only the linear region for $r \geq 2$ mm, where sensitivity to thermal conductivity is maximized and any aberrations near $r = 0$ mm can be neglected. An example fit of diamond is shown in the inset of Fig. 4(c) for a modulation frequency of 24 Hz.

We note that the thermal conductivities of the materials measured in this study are modeled as isotropic when performing a model fit. Thus, the $\kappa_{measured}$ value is representative of an isotropic value. However, anisotropic materials could be handled in a similar manner as in thermoreflectance experiments.[25] In particular, either the in-plane or cross-plane thermal conductivity could be fitted. We generally find significantly higher sensitivity to the in-plane thermal spreading and, therefore, the in-plane thermal conductivity.

TABLE II. Measured thermal conductivities compared with literature values. For reference, we also list the heat capacity, thickness, and radius of each sample. The fused silica, sapphire, germanium, and silicon samples were purchased from Thorlabs. The copper was purchased from McMaster-Carr, and the diamond was supplied by Element Six.

Sample	Manufacturer no.	$\kappa_{Meas.}$ (W m^{-1} K^{-1})	$\kappa_{Ref.}$ (W m^{-1} K^{-1})	C (MJ m^{-3} K^{-1})	d (mm)	r_{sample} (mm)
Fused silica	PF10-03	1.46 ± 0.10	1.38[7]	1.63[24]	6.12	12.66
Sapphire	WG31050	35.4 ± 3.4	33.4[7]	3.06[25]	4.85	12.65
Germanium	WG91050	54.5 ± 5.5	55.7[7]	1.72[26]	5.00	12.69
Silicon	WG81050	142 ± 19	148[27]	1.65[24]	5.08	12.67
Copper	9103K2	385 ± 35	398[28]	3.45[28]	12.70	25.4
Diamond	TM220	2490 ± 310	2200[a]	1.78[29]	1.27	16.5

[a]Manufacturer-specified value.

© Author(s) 2026

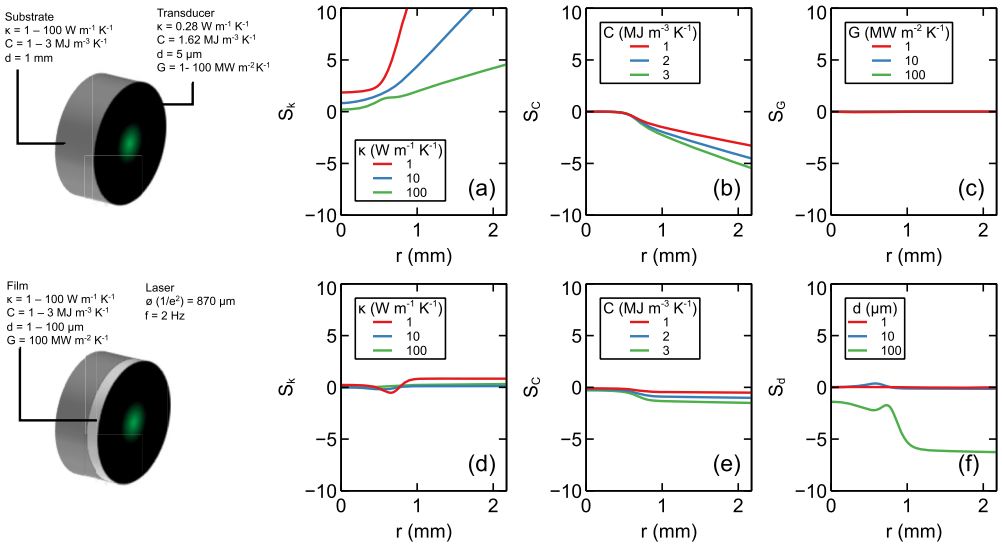


FIG. 6. Sensitivity, S_x, of the phase to a given parameter, x, as a function of radius. Plots (a)–(c) display sensitivities for a transducer/substrate sample stack. In this case, the sample is assumed to have a thermal conductivity, heat capacity, and thermal boundary conductance of 100 W m^{-1} K^{-1}, 2 MJ m^{-3} K^{-1}, and 1 MW m^{-2} K^{-1}, respectively, unless otherwise noted. Plots (d)–(f) correspond to a transducer/film/substrate stack. The same substrate conditions are assumed, and the film is assumed to have a thermal conductivity, heat capacity, and thickness of 1 W m^{-1} K^{-1}, 2 MJ m^{-3} K^{-1}, and 50 μm, unless otherwise noted. The front- and back-side thermal boundary conductances are assumed to be 1 and 100 MW m^{-2} K^{-1}, respectively.

However, for certain sample geometries such as thin foils or membranes, or for highly anisotropic materials, there can also be sensitivity to cross-plane spreading.

Sensitivity to heat capacity shows a trend similar in magnitude but opposite in sign to that of thermal conductivity. This occurs because the measurement is fundamentally sensitive to thermal diffusivity, with thermal conductivity and heat capacity having opposite effects on the frequency-dependent thermal response.[10] Therefore, the heat capacity and thermal conductivity cannot be simultaneously fit; one parameter or the other must be assumed. We tabulate the heat capacity values assumed in these measurements in Table II.

We also show sensitivity to the interface conductance between the PET/substrate in Fig. 6(c) for $1 \leq G \leq 100$ MW m^{-2} K^{-1}. In short, there is minimal sensitivity to the interface. We assume a comparably low value (e.g., 1 MW m^{-2} K^{-1}) for the adhesive/substrate interface relative to the metal transducer/substrate interface conductance found in thermoreflectance samples (which are generally on the order of 10^1–10^2 MW m^{-2} K^{-1}).[33–35] However, the assumption for G yields minimal impact on the fitted thermal conductivity. The lack of sensitivity can be attributed to the much larger (millimeter) spatial scales of the measurement compared to the microscale heater radius and thermal diffusion depths of thermoreflectance.

While the measurements in this study are of bulk substrates, we also consider the sensitivity of the technique for a film-on-substrate shown in Figs. 6(d)–6(f). For the substrate, we assume the same default thermal properties mentioned previously. For the film, we assume front- and back-side thermal boundary conductances of 1 and 100 MW m^{-2} K^{-1}, respectively. The default thermal conductivity, heat capacity, and thickness of the film are assumed to be 1 W m^{-1} K^{-1}, 2 MJ m^{-3} K^{-1}, and 50 μm, respectively. Compared to the bulk substrate, there is significantly lower sensitivity to the thermal conductivity and heat capacity despite the assumed value. This can again be attributed to the large spatial extent of the measurement's thermal diffusion length relative to the thermal resistance of the film. For this example, there is no appreciable sensitivity to the film until the thickness is on the order of tens of microns, or greater. One approach to enhance the measurement of thin films is by minimizing the substrate thickness (e.g., via polishing or lapping the substrate) until a point where $S_{\kappa_{\text{film}}} > S_{\kappa_{\text{substrate}}}$. Alternatively, the substrate may be removed completely and the film probed directly as a suspended membrane.[36,37]

V. SUMMARY

In summary, we discuss a thermal metrology approach that combines principles of established lock-in IR thermography and thermoreflectance analysis to enable wide-range thermal conductivity measurements while overcoming several experimental limitations. The approach is non-contact, requires only single-sided sample access (heating and measurements both occur on the front side), and is tolerant of surface roughness. We demonstrate that an absorbing layer is not required; however, a thin, removable PET adhesive reduces incident power requirements. We also discuss limitations of the technique, with regard to equipment requirements and measurement sensitivity. Ultimately, we validate this approach by measuring an array of materials with thermal conductivities spanning three orders of magnitude, reaching $\kappa > 2000$ W m^{-1} K^{-1}, in agreement with literature values.

© Author(s) 2026

ACKNOWLEDGMENTS

The authors are grateful to Element Six for providing the diamond wafer for thermal analysis. Research at the Naval Research Laboratory was partially supported by the Office of Naval Research. J.R. and P.E.H. appreciate support from the Office of Naval Research under Grant No. N00014-23-1-2630. E.A.S., J.L.B., and J.T.G. appreciate support from the Department of War through the STTR Program under Grant No. N68335-25-C-0590.

AUTHOR DECLARATIONS

Conflict of Interest

The authors have no conflicts to disclose.

Author Contributions

Ethan A. Scott: Conceptualization (lead); Data curation (lead); Formal analysis (lead); Investigation (lead); Methodology (lead); Writing – original draft (lead). **Jeffrey L. Braun**: Investigation (supporting); Resources (supporting); Validation (equal); Writing – review & editing (supporting). **Jessica Reyes**: Investigation (supporting); Writing – review & editing (supporting). **Bruce Bolliger**: Resources (supporting); Writing – review & editing (supporting). **Terrence Soares**: Resources (supporting); Writing – review & editing (supporting). **John T. Gaskins**: Funding acquisition (supporting); Resources (supporting); Writing – review & editing (supporting). **Marko J. Tadjer**: Resources (supporting); Writing – review & editing (supporting). **Patrick E. Hopkins**: Conceptualization (equal); Funding acquisition (lead); Investigation (equal); Project administration (equal); Resources (lead); Writing – review & editing (supporting).

DATA AVAILABILITY

The data that support the findings of this study are available from the corresponding author upon reasonable request.

APPENDIX A: FREQUENCY-DOMAIN THERMAL MODEL FOR LOCK-IN INFRARED THERMOGRAPHY

Our LIT analysis is based upon a radially symmetric solution of the multilayer heat diffusion equation in the frequency domain, similar to models used for thermoreflectance analysis.[2,15,18] Ultimately, this model computes the thermal phase, $\theta(r,\omega)$, from the complex surface temperature response, $\tilde{T}(r,\omega)$, generated by a periodically modulated Gaussian laser heating source.

A key feature of this formulation is that two transforms are applied: (i) a Fourier transform in time and (ii) a Hankel transform in the radial coordinate. Throughout this appendix, we adopt the same transform notation from Braun *et al.*[2,19] That is,

- A tilde above a variable (e.g., $\tilde{T}$) denotes a Fourier-transformed quantity.
- A tilde below a variable (e.g., $\underset{\sim}{T}$) denotes a Hankel-transformed quantity.
- A variable with both (e.g., $\underset{\sim}{\tilde{T}}$) is transformed in both domains.

1. Frequency-domain heat diffusion equation

We begin by considering the time- and space-dependent temperature distribution in a material, which is governed by the heat equation,

$$\rho c_p \frac{\partial T}{\partial t} = \nabla \cdot (\boldsymbol{\kappa} \nabla T), \tag{A1}$$

where ρc_p is the volumetric heat capacity and $\boldsymbol{\kappa}$ is the thermal conductivity tensor. For an axisymmetric system with radial and cross-plane conductivities κ_r and κ_z, respectively,

$$\rho c_p \frac{\partial T}{\partial t} = \kappa_r \left(\frac{\partial^2 T}{\partial r^2} + \frac{1}{r}\frac{\partial T}{\partial r} \right) + \kappa_z \frac{\partial^2 T}{\partial z^2}. \tag{A2}$$

The laser heating is modulated at an angular frequency ω. Because the heat equation is linear, the temperature response can be expressed as a Fourier series. For a single modulation frequency, the temperature can be written as

$$T(r,z,t) = \mathrm{Re}\left[\tilde{T}(r,z,\omega)\, e^{i\omega t}\right]. \tag{A3}$$

Here, $\tilde{T}(r,z,\omega)$ is the complex temperature amplitude at frequency ω. It encodes both the oscillation magnitude and phase. The experimentally measured temperature oscillation corresponds to the real part of this expression, while the phase is obtained from the complex argument of $\tilde{T}(r,z,\omega)$.

Substituting this expression into the heat equation yields the frequency-domain form

$$i\omega \rho c_p \tilde{T} = \kappa_r \left(\frac{\partial^2 \tilde{T}}{\partial r^2} + \frac{1}{r}\frac{\partial \tilde{T}}{\partial r} \right) + \kappa_z \frac{\partial^2 \tilde{T}}{\partial z^2}, \tag{A4}$$

which describes the spatial variation of the complex temperature field at a single modulation frequency.

2. Hankel transform

Because the system is radially symmetric, the radial dependence can be simplified using a zeroth-order Hankel transform. The transform is defined as

$$\mathcal{H}_0\{f(r)\} = \underset{\sim}{f}(k) = \int_0^\infty f(r)\, J_0(kr)\, r\, dr, \tag{A5}$$

where J_0 is the zeroth-order Bessel function and k is the radial wavenumber.

Applying this transform to the Fourier-domain temperature gives

$$\underset{\sim}{\tilde{T}}(k,z,\omega) = \int_0^\infty \tilde{T}(r,z,\omega) J_0(kr)\, r\, dr. \tag{A6}$$

The Hankel transform converts the radial Laplacian into an algebraic term,

$$\mathcal{H}_0\left[\frac{\partial^2 \tilde{T}}{\partial r^2} + \frac{1}{r}\frac{\partial \tilde{T}}{\partial r} \right] = -k^2 \underset{\sim}{\tilde{T}}. \tag{A7}$$

© Author(s) 2026

Substituting into the heat equation yields

$$\kappa_z \frac{\partial^2 \tilde{T}}{\partial z^2} - \left(\kappa_r k^2 + i\omega\rho c_p\right)\tilde{T} = 0. \tag{A8}$$

Thus, the original partial differential equation reduces to an ordinary differential equation in the depth coordinate z.

3. Thermal wavevector

We next define a complex thermal wavevector,

$$q = \sqrt{\frac{\kappa_r k^2 + i\omega\rho c_p}{\kappa_z}}, \tag{A9}$$

so that the governing equation may be simplified as

$$\frac{\partial^2 \tilde{T}}{\partial z^2} - q^2 \tilde{T} = 0. \tag{A10}$$

At this point, we note that the solution may be first obtained in Hankel space, where the depth dependence can be solved analytically. Then, the radial temperature distribution can subsequently be obtained using the inverse Hankel transform.

4. Multilayer transfer matrix formulation

To generalize the solution to multilayered systems, we use a transfer matrix formalism that relates temperature and heat flux at the top and bottom of each layer.[2,19] In the following notation, we define a multilayered system as an n-layered stack, where each layer is assigned an index, i. The top (surface) layer of the sample stack is defined as $i = 1$ and the bottom (substrate) layer as $i = n$.

The depth-dependent, transformed heat flux applied to the sample is defined as

$$\tilde{Q} = -\kappa_z \frac{\partial \tilde{T}}{\partial z}. \tag{A11}$$

For layer i,

$$\begin{bmatrix} \tilde{T}_{b,i} \\ \tilde{Q}_{b,i} \end{bmatrix} = \mathbf{M}_i \begin{bmatrix} \tilde{T}_{t,i} \\ \tilde{Q}_{t,i} \end{bmatrix}, \tag{A12}$$

where the subscripts b and t refer to the bottom and top of the layer, respectively. The layer transfer matrix is

$$\mathbf{M}_i = \begin{bmatrix} \cosh(q_i d_i) & -\dfrac{\sinh(q_i d_i)}{\kappa_{z,i} q_i} \\ -\kappa_{z,i} q_i \sinh(q_i d_i) & \cosh(q_i d_i) \end{bmatrix}. \tag{A13}$$

Thermal boundary resistance between adjacent layers is incorporated using

$$\mathbf{N}_i = \begin{bmatrix} 1 & -1/G_i \\ 0 & 1 \end{bmatrix}, \tag{A14}$$

where G_i is the thermal boundary conductance between layers i and $i + 1$.

The full multilayer transfer matrix is then obtained by multiplying the matrices of all individual layers and interfaces,

$$\begin{bmatrix} \tilde{A} & \tilde{B} \\ \tilde{C} & \tilde{D} \end{bmatrix} = \mathbf{M}_n \mathbf{N}_{n-1} \mathbf{M}_{n-1} \cdots \mathbf{N}_2 \mathbf{M}_2 \mathbf{N}_1 \mathbf{M}_1. \tag{A15}$$

Although the layer indices increase from the surface $(i = 1)$ into the substrate $(i = n)$, the transfer matrices are multiplied in reverse order so that the resulting matrix relates the temperature and heat flux at the top and bottom of the multilayer structure.

With this, the temperature and heat flux at the top and bottom of the entire structure may be related by

$$\begin{bmatrix} \tilde{T}_b \\ \tilde{Q}_b \end{bmatrix} = \begin{bmatrix} \tilde{A} & \tilde{B} \\ \tilde{C} & \tilde{D} \end{bmatrix} \begin{bmatrix} \tilde{T}_t \\ \tilde{Q}_t \end{bmatrix}. \tag{A16}$$

5. Surface response

To obtain a solution for the surface response, a bottom boundary condition must be applied. For an adiabatic bottom boundary,

$$\tilde{Q}_b = 0. \tag{A17}$$

Applying this condition yields

$$\frac{\tilde{T}_t}{\tilde{Q}_t} = -\frac{\tilde{D}}{\tilde{C}}. \tag{A18}$$

For reference, we note that the assumption of an adiabatic bottom boundary condition is reasonable for the materials tested in this work; including air as an additional layer in the multilayered model negligibly affects the surface response.

6. Gaussian heating and inverse transform

The next step in obtaining the surface temperature response is to account for the surface heat flux term, $\tilde{Q}_t$. This heat flux is provided by the absorbed laser heating. For a Gaussian laser beam with a $1/e^2$ radius of w_0, the spatial distribution of the absorbed laser heating is[18]

$$Q(r) = \frac{2A_0}{\pi w_0^2} \exp\left(-\frac{2r^2}{w_0^2}\right), \tag{A19}$$

where A_0 is the amplitude of the absorbed modulated laser power. For a periodically modulated pump beam, the absorbed power can be expressed as[19]

$$A(t) = A_0(e^{i\omega t} + 1), \tag{A20}$$

where the first term represents the modulated component at angular frequency ω. The steady-state component does not contribute to the lock-in signal and is neglected.[2] Thus, the modulated component of the heat flux can be written in the standard Fourier form

$$Q_{AC}(r,t) = \tilde{Q}(r,\omega)e^{i\omega t}, \tag{A21}$$

© Author(s) 2026

where $\tilde{Q}(r,\omega)$ is the complex Fourier amplitude of the heat flux, i.e.,

$$\tilde{Q}(r,\omega) = \frac{2A_0}{\pi w_0^2}\exp\left(-\frac{2r^2}{w_0^2}\right). \tag{A22}$$

The zeroth-order Hankel transform of the Gaussian heating profile is then calculated as

$$\tilde{Q}(k,\omega) = \frac{A_0}{2\pi}\exp\left(-\frac{k^2 w_0^2}{8}\right). \tag{A23}$$

The complex surface temperature response is then obtained by multiplying the surface thermal response function by the transformed heat flux and performing the inverse Hankel transform,

$$\tilde{T}(r,\omega) = \frac{A_0}{2\pi}\int_0^\infty \left(-\frac{\tilde{D}}{\tilde{C}}\right)\exp\left(-\frac{k^2 w_0^2}{8}\right)J_0(kr)k\,dk. \tag{A24}$$

The integral is evaluated numerically using Gauss–Legendre quadrature,

$$\int_a^b f(k)\,dk \approx \sum_{m=1}^{N_q} w_m f(k_m), \tag{A25}$$

where k_m and w_m are the quadrature nodes and weights, respectively, and N_q is the number of quadrature points.[25] We find 500 quadrature points and an upper integration limit of $\frac{10}{w_0}$ to be sufficient for convergence under the measurement conditions of this work.

The resulting $\tilde{T}(r,\omega)$ represents the complex Fourier amplitude of the temperature oscillation at the modulation frequency. [For reference, we note that the physical surface temperature oscillation can be obtained from $T(r,t) = \mathrm{Re}\left[\tilde{T}(r,\omega)e^{i\omega t}\right]$. However, the lock-in phase is determined from the complex phase of $\tilde{T}(r,\omega)$.]

7. Parameter fitting and uncertainty

Finally, the modeled phase is computed from the complex temperature,

$$\theta(r,\omega) = \mathrm{atan2}\left(\mathrm{Im}[\tilde{T}(r,\omega)], \mathrm{Re}[\tilde{T}(r,\omega)]\right), \tag{A26}$$

and the model is fit to experimental data by minimizing the sum of squared errors,

$$SSE = \sum_j \left[\theta_{\mathrm{exp}}(r_j,\omega) - \theta_{\mathrm{model}}(r_j,\omega)\right]^2, \tag{A27}$$

where j indexes the discrete radial positions in the measured and modeled phase profiles.

APPENDIX B: PEAK AND AREA-AVERAGED LOCK-IN TEMPERATURE AMPLITUDES

The peak temperature amplitude is monitored with the lock-in camera. We adjust the laser power to provide a sufficient signal-to-noise ratio while limiting self-heating. In this implementation, we limit the peak lock-in temperature amplitude to $|\tilde{T}(r=0,\omega)| < 20$ K; the corresponding area-averaged measured lock-in temperature amplitude is less than 1 K. We define $T_{\mathrm{avg}}(\omega)$ as the measured lock-in temperature amplitude averaged over the sample area contained within the radial phase-fit region ($r_{\min}$ to $r_{\max}$), with each radial position weighted by its annular area $2\pi r dr$. This is calculated as

$$T_{\mathrm{avg}}(\omega) = \frac{\int_{r_{\min}}^{r_{\max}} |\tilde{T}(r,\omega)|\,2\pi r\,dr}{\int_{r_{\min}}^{r_{\max}} 2\pi r\,dr} = \frac{2}{r_{\max}^2 - r_{\min}^2}\int_{r_{\min}}^{r_{\max}} |\tilde{T}(r,\omega)|\,r\,dr. \tag{B1}$$

When $r_{\min} = 0$, this reduces to

$$T_{\mathrm{avg}}(\omega) = \frac{2}{r_{\max}^2}\int_0^{r_{\max}} |\tilde{T}(r,\omega)|\,r\,dr. \tag{B2}$$

REFERENCES

[1] T. W. Pfeifer, H. B. Schonfeld, E. A. Scott, H. T. Aller, J. T. Gaskins, D. H. Olson, J. L. Braun, S. Graham, and P. E. Hopkins, Annu. Rev. Mater. Res. **55**, 37 (2025).
[2] J. L. Braun, D. H. Olson, J. T. Gaskins, and P. E. Hopkins, Rev. Sci. Instrum. **90**, 024905 (2019).
[3] R. C. Kerschbaumer, S. Stieger, M. Gschwandl, T. Hutterer, M. Fasching, B. Lechner, L. Meinhart, J. Hildenbrandt, B. Schrittesser, P. F. Fuchs, G. R. Berger, and W. Friesenbichler, Polym. Test. **80**, 106121 (2019).
[4] D. J. Twitchen, C. S. J. Pickles, S. E. Coe, R. S. Sussmann, and C. E. Hall, Diamond Relat. Mater. **10**, 731 (2001).
[5] Y. Yamamoto, T. Imai, K. Tanabe, T. Tsuno, Y. Kumazawa, and N. Fujimori, Diamond Relat. Mater. **6**, 1057 (1997).
[6] R. Sundar and C. Sudha, Int. J. Thermophys. **46**, 13 (2025).
[7] J. L. Braun, B. N. Baines, J. T. Gaskins, and P. E. Hopkins, Rev. Sci. Instrum. **96**, 074901 (2025).
[8] A. U. Gaitonde, A. A. Candadai, J. A. Weibel, and A. M. Marconnet, Rev. Sci. Instrum. **94**, 074904 (2023).
[9] A. Bedoya, E. Marín, J. J. Puldón, and C. García-Segundo, Int. J. Thermophys. **44**, 27 (2023).
[10] A. Bedoya, A. Salazar, A. Mendioroz, and E. Marín, J. Appl. Phys. **135**, 135102 (2024).
[11] A. Salazar and A. Mendioroz, Int. J. Therm. Sci. **214**, 109928 (2025).
[12] Á. Cifuentes, A. Mendioroz, and A. Salazar, Int. J. Therm. Sci. **121**, 305 (2017).
[13] Y. Kaneko, R. Fujita, T. Ishizaki, and H. Nagano, Int. J. Thermophys. **46**, 50 (2025).
[14] T. Ishizaki and H. Nagano, Infrared Phys. Technol. **99**, 248 (2019).
[15] A. J. Schmidt, R. Cheaito, and M. Chiesa, Rev. Sci. Instrum. **80**, 094901 (2009).
[16] P. Jiang, X. Qian, and R. Yang, J. Appl. Phys. **124**, 161103 (2018).
[17] D. J. Kirsch, J. Martin, R. Warzoha, M. McLean, D. Windover, and I. Takeuchi, Rev. Sci. Instrum. **95**, 103006 (2024).
[18] D. G. Cahill, Rev. Sci. Instrum. **75**, 5119 (2004).
[19] J. L. Braun and P. E. Hopkins, J. Appl. Phys. **121**, 175107 (2017).
[20] J. Yang, E. Ziade, and A. J. Schmidt, Rev. Sci. Instrum. **87**, 014901 (2016).
[21] X. Xie, D. Li, T.-H. Tsai, J. Liu, P. V. Braun, and D. G. Cahill, Macromolecules **49**, 972 (2016).
[22] J. Yang, E. Ziade, and A. J. Schmidt, J. Appl. Phys. **119**, 095107 (2016).
[23] A. Wolf, P. Pohl, and R. Brendel, J. Appl. Phys. **96**, 6306 (2004).
[24] E. A. Scott, S. W. Smith, M. D. Henry, C. M. Rost, A. Giri, J. T. Gaskins, S. S. Fields, S. T. Jaszewski, J. F. Ihlefeld, and P. E. Hopkins, Appl. Phys. Lett. **113**, 192901 (2018).
[25] E. Ziade, Rev. Sci. Instrum. **91**, 124901 (2020).
[26] J. Paterson, D. Singhal, D. Tainoff, J. Richard, and O. Bourgeois, J. Appl. Phys. **127**, 245105 (2020).
[27] W. Liu and M. Asheghi, J. Heat Transfer **128**, 75 (2005).

© Author(s) 2026

[28]C. Cancellieri, E. A. Scott, J. Braun, S. W. King, R. Oviedo, C. Jezewski, J. Richards, F. La Mattina, L. P. H. Jeurgens, and P. E. Hopkins, J. Appl. Phys. **128**, 195302 (2020).
[29]E. A. Scott, J. L. Braun, K. Hattar, J. D. Sugar, J. T. Gaskins, M. Goorsky, S. W. King, and P. E. Hopkins, J. Appl. Phys. **129**, 055307 (2021).
[30]J. Yang, C. Maragliano, and A. J. Schmidt, Rev. Sci. Instrum. **84**, 104904 (2013).
[31]A. Mendioroz, R. Fuente-Dacal, E. Apiñaniz, and A. Salazar, Rev. Sci. Instrum. **80**, 074904 (2009).
[32]L. Fabbri and P. Fenici, Rev. Sci. Instrum. **66**, 3593 (1995).
[33]R. Cheaito, J. T. Gaskins, M. E. Caplan, B. F. Donovan, B. M. Foley, A. Giri, J. C. Duda, C. J. Szwejkowski, C. Constantin, H. J. Brown-Shaklee, J. F. Ihlefeld, and P. E. Hopkins, Phys. Rev. B **91**, 035432 (2015).
[34]H. T. Aller, J. A. Malen, and A. J. H. McGaughey, Phys. Rev. Appl. **15**, 064043 (2021).
[35]C. Monachon, L. Weber, and C. Dames, Annu. Rev. Mater. Res. **46**, 433 (2016).
[36]F. Jiang, M. Ryu, V. Pachauri, S. Ingebrandt, X. T. Vu, and J. Morikawa, Rev. Sci. Instrum. **94**, 094903 (2023).
[37]A. Alasli, R. Iguchi, K.-i. Uchida, and H. Nagano, Appl. Phys. Lett. **126**, 044102 (2025).

© Author(s) 2026